Journal of Electronics and Electrical Engineering
https://ojs.wiserpub.com/index.php/JEEE

Research Article

Mapping Radar Cross-Section Hotspots with Statistical Characterization & Detection Probability Analysis of Stealth Aircraft

Muhammad Abdullah*, **Jungang Miao**

School of Electronic and Information Engineering, Beihang University, Beijing 100191, China
* Correspondence: muham_ab@buaa.edu.cn

Received: 17 March 2026; **Revised:** 9 June 2026; **Accepted:** 23 June 2026; **Published:** 29 June 2026

Abstract: The Radar Cross Section (RCS) of stealth aircraft exhibits strong dependence on azimuth angle, requiring a statistical approach for analyzing probability of detection under variable illumination conditions. This study investigates the RCS behavior of the B-2 Spirit at 300 MHz under monostatic and bistatic radar configurations incorporating both vertical and horizontal polarizations. High-resolution RCS simulations are performed using a validated CAD model, and heatmaps are generated to identify angular regions that exhibit peak scattering. These scattering hotspots are shown to occur only at specific incidence angles, strongly influencing detection outcomes. To statistically quantify this behavior, the RCS data are segmented into angular sectors and modeled with simple unimodal distributions. Probability of detection is estimated using Monte Carlo simulations across all sectors under varying signal-to-noise ratios. The results reveal that certain bistatic configurations achieve higher detection probabilities at lower SNRs compared to monostatic setups, emphasizing the role of geometrical diversity in enhancing stealth detectability. Furthermore, small variations in illumination angle produce large differences in detection performance, reflecting the aerodynamic and structural shaping strategies used in stealth design. These findings highlight the importance of localized statistical characterization for stealth targets and offer a foundation for optimizing radar deployment and detection strategy planning in operational scenarios.

***Keywords*:** bistatic, monostatic, probability of detection, Radar Cross Section (RCS) characterization, stealth aircraft

1. Introduction

The electromagnetic scattering behavior of a complex object is influenced by a multitude of factors, including the object's size relative to the illuminating wavelength, its material composition, the operational bandwidth, polarization state, and the viewing geometry of both the radar transmitter and receiver [1–6]. Additionally, dynamic structural features such as rotating components, airframe flexibility, and both fixed and movable electronic antennas contribute to time-varying scattering, especially during maneuvering flight. These effects collectively necessitate detailed simulations and measurements to accurately characterize the target's scattering signature from the standpoint of radar system performance analysis. Since the early development of radar in the 1930s, reducing the Radar Cross Section (RCS) has remained a fundamental goal in military aircraft design [7].

Stealth platforms achieve low observability through geometric shaping that reflects incident energy away from receivers and through frequency-dependent Radar Absorbing Materials (RAM) that attenuate surface currents. The F-117

DOI: https://doi.org/10.37256/jeee.5120269903

achieves this via its faceted body [8], while the B-2 Spirit bomber uses a blended wing-body configuration and embedded engine inlets to reduce specular returns [9]. Conventional radar detection is further challenged by advances in low-frequency and Over-the-Horizon (OTH) radar systems [10], especially those operating in the VHF and UHF bands. While these radars exploit long wavelengths to counter stealth shaping, their deployment is often constrained by large antenna apertures and ionospheric propagation effects. Moreover, detection is probabilistic by nature, particularly when aircraft orientation changes rapidly or the radar illumination is stochastic.

In 1947, Marcum [11] derived the probability of detection (P_d) for non-fluctuating targets in Gaussian noise, which was later generalized by Swerling [12] to incorporate RCS fluctuations using Rayleigh (Swerling I & II are actually negative exponential in power but since the power is exponentially distributed, the signal amplitude which is square root of power follows a Rayleigh distribution) and chi-square (χ^2) models (Swerling III & IV are χ-fourth order in amplitude, which translates to a χ^2-fourth order distribution when discussing the power of signal). Since then, several statistical distributions such as Log-Normal (LOGN), Weibull (WEIB) and Rice etc. have been employed to model RCS variability [13–21]. However, most models are evaluated globally across all angles failing to capture the aspect-dependent scattering behavior of stealth aircraft. For example, RCS of the B-2 Spirit could exhibit strong angular dependence due to blended geometries and subtle discontinuities such as trailing edges and internal cavity gaps which can contribute to observable scattering at specific incident directions. This necessitates angularly localized statistical characterization particularly under varying radar configurations and polarizations. Although prior literature has explored monostatic RCS profiles and fitted parametric models for individual stealth aircraft [22–27], limited work exists on bistatic RCS analysis under statistical modeling frameworks. Moreover, the effect of Signal-to-Noise Ratio (SNR) variations on detection performance is rarely incorporated in a localized angular context. These gaps motivate a comprehensive treatment of aspect-resolved RCS modeling and detectability analysis particularly for VHF/UHF frequencies and for both HH and VV polarizations.

In this study, we simulate the monostatic and bistatic RCS of the B-2 Spirit aircraft at 200 MHz, 300 MHz and 400 MHz using CST Studio Suite [28]. The CAD model is validated using multi-solver consistency checks to ensure reproducibility and physical integrity. We perform the analysis under HH and VV polarizations with and without RAM coatings modeled using frequency-dispersive material parameters. Key contributions of this work include:

(a) Heat-map visualization of angular scattering hotspots in both monostatic and bistatic configurations to identify dominant aspect-dependent scattering centers.

(b) Angular-sector-based statistical characterization of RCS using three unimodal distributions: LOGN, WEIB and beta (β) distributions.

(c) Monte Carlo-based estimation of the P_d across segmented angular sectors allowing detection performance mapping under varying SNR conditions.

(d) Comparative evaluation of P_d and scattering patterns between monostatic and bistatic configurations identifying angular zones where stealth performance degrades significantly.

(e) Introduction of an Entropy-based Detection Complexity Index (EDCI) which quantifies the spatial scattering complexity in each angular sector. This metric correlates with detection difficulty and provides new insight into the radar sensitivity and information content embedded in each observation angle. High-entropy sectors generally correspond to highly fluctuating scattering sectors while low-entropy sectors indicate stable echo returns.

2. RCS statistical analysis of stealth aircraft

2.1 *Selection of CAD model of aircraft*

Accurate electromagnetic simulation of advanced stealth platforms such as the B-2 Spirit presents several non-trivial challenges. Foremost among them is the unavailability of authentic Digital Mock-Up (DMU) models, as real-world stealth aircraft geometries are typically classified. Consequently, researchers must often rely on open-source 3D CAD models that approximate the external shape of such platforms. However, these aftermarket models are frequently unsuitable for Computational Electromagnetic (CEM) analysis in their raw form, due to issues like open surfaces, intersecting geometries, broken edges or topological inconsistencies that violate the geometric requirements of full-wave solvers. Another significant limitation arises from the lack of robust RAM property libraries in CEM tools. While RAM contributes to RCS suppression, typically by 20%–30% [29], the majority of signature reduction (up to 70%-80%) is achieved through shaping. Therefore, a validated geometric model that accurately represents scattering features becomes paramount.

To ensure simulation fidelity, we adopted a structured preprocessing and validation pipeline. First, the open-source CAD model underwent geometry healing operations to eliminate topological defects making it compatible with CST Studio Suite (performed by CST Studio Suite). Second, the preprocessed model was simulated using multiple electromagnetic solvers, including the Asymptotic Solver (AS) [30] (based on Shooting and Bouncing Ray (SBR) method) and Integral Equation (IE) solvers (using Multilevel Fast Multipole Method (MLFMM) [31]) across identical angular sweeps. A model was only accepted for further use if it exhibited solver-consistent RCS trends, indicating numerical stability and convergence. This solver-level cross-validation serves as a practical proxy for geometric fidelity and confirms that primary scattering mechanisms (e.g., edge diffraction, creeping waves, specular returns) are preserved.

Figure 1A presents the CAD model of the B-2 Spirit stealth bomber aircraft, while Figure 1B illustrates the spherical coordinate convention used to compute its RCS. The simulations are conducted in a monostatic configuration at 300 MHz using CST Studio Suite, where the radar line-of-sight is swept azimuthally ($\phi = 0^\circ$ to 360°) in the x-y plane with a fixed elevation angle of $\theta = 90^\circ$. The monostatic RCS is computed using two distinct electromagnetic solvers, AS based on the SBR method and the full-wave IE solver accelerated via the MLFMM. The results are shown in Figure 2 for both VV and HH polarizations and statistical summaries are reported in Table 1. From Table 1, we observe that the AS method consistently yields higher mean RCS values and larger standard deviations compared to MLFMM. For instance, in VV polarization, the AS method results in a mean RCS of 2.0596 m^2 (3.14 dBsm), while MLFMM yields 0.9152 m^2 (−0.38 dBsm). A similar trend holds for HH polarization, where the AS Method produces a mean of 5.2803 m^2 (7.23 dBsm) versus 2.5039 m^2 (3.99 dBsm) from MLFMM [32].

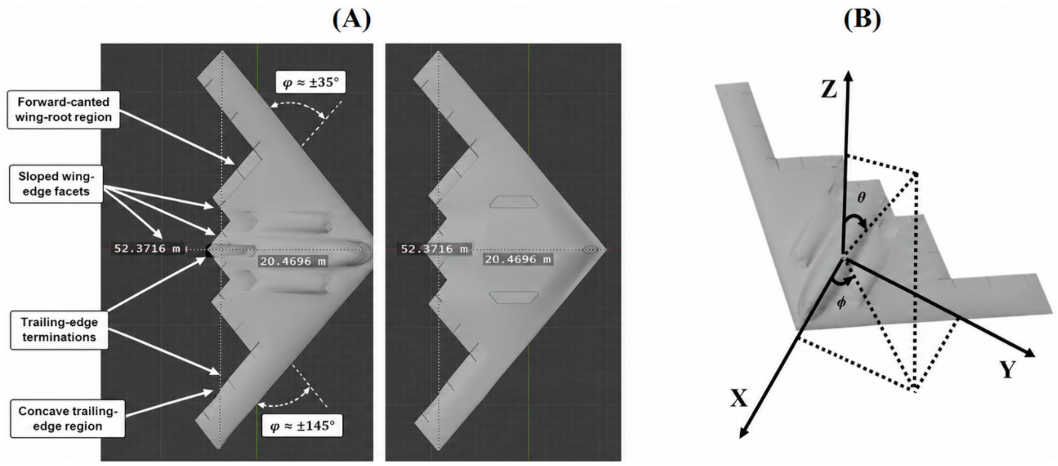

Figure 1. CAD model of the B-2 Spirit stealth aircraft with dimensions and scattering-relevant geometric features. (A) Top and bottom views of the aircraft, including annotated forward-canted wing-root regions, sloped wing-edge facets, and trailing-edge terminations associated with dominant angular scattering responses. The wingspan of the aircraft is 52.37 m and the length is 20.47 m [33]; (B) Coordinate system used for RCS simulations

The differences in the mean values are mathematically justified by the underlying formulation of each solver [34]. CST's AS Method is based on the SBR technique which uses high-frequency approximations of Maxwell's equations and assumes Geometrical Optics (GO) and Physical Optics (PO) scattering. The total scattered field E_{scat} in SBR is given by

$$E_{scat} = E_{GO}(r) + E_{PO}(r) \tag{1}$$

where E_{GO} accounts for specular reflections from large facets and E_{PO} includes surface currents induced on illuminated surfaces. The method ignores low-frequency effects like creeping waves and mutual coupling leading to overestimation of RCS especially at angles where GO reflections dominate. In contrast, the MLFMM solver numerically solves Electric Field Integral Equations (EFIE) or Combined Field Integral Equations (CFIE) based on surface current densities $J(r)$ using:

$$\widehat{n}\times\left[E_{inc}(r)+j\omega\mu\int_{S}G\left(r,\ r'\right)\cdot J(r')dS'\right]=0 \tag{2}$$

where $G\left(r,\ r'\right)$ is the dyadic Green's function.

Table 1. B-2 aircraft monostatic RCS values for model validation

f^a	Pol	parameter	AS method		IE solver MLFMM	
			m^2	dbsm	m^2	dbsm
300 MHz	VV	mean	2.0596	3.1379	0.9152	−0.3846
		std	4.7457	6.7630	2.1715	3.3676
	HH	mean	5.2803	7.2266	2.5039	3.9861
		std	21.0686	13.2343	8.6147	9.3524

[a] f = frequency, pol = Polarization, AS = Asymptotic Solver, IE = Integral Equation, Multilevel Fast Multipole Method = MLFMM

MLFMM efficiently handles mutual interactions between mesh elements and captures near-field effects such as creeping waves and edge diffraction. This leads to a more physically accurate yet conservative RCS estimate, especially at lower frequencies where wave phenomena dominate over GO. However, this improved physical fidelity is achieved at the cost of increased computational time. The simulation plots shown in Figure 2 further illustrate solver behavior. Prominent RCS peaks are observed at $\phi \approx \pm 35^\circ$ and $\phi \approx \pm 145^\circ$ in both solvers [35, 36]. These azimuth angles align with the forward-canted wing roots and trailing edge terminations of the B-2 Spirit's blended-wing-body geometry. The spike at $\pm 35^\circ$ likely corresponds to forward-scattering lobe enhancements where the incident wave-front aligns with sloped wing-edge facets generating constructive surface current interference. Conversely, the peaks near $\pm 145^\circ$ are attributed to backscattering from concave trailing edge regions where energy is focused and retro-reflected due to grazing incidence and concavity-induced multiple bounces, phenomena well captured in SBR and partially in MLFMM. These physical RCS features demonstrate that despite differing solver formulations both methods identify consistent angular hotspots in the RCS profile. This alignment across methods enhances confidence in the geometric validity of the preprocessed CAD model. Moreover, the peak locations match well-known scattering zones of the B-2 aircraft, as reported in the limited available computational literature [36]. Taken together, the multi-solver analysis, employing both ray-based and MLFMM, validates that our open-source CAD model, after topological corrections, produces physically meaningful RCS signatures. This multi-solver cross-verification constitutes a core component of our RCS validation strategy. While a full electromagnetic design and fabrication activity would require significantly more resources and classified specifications, which are beyond the scope of this study, our methodology offers a reproducible approach for academic research.

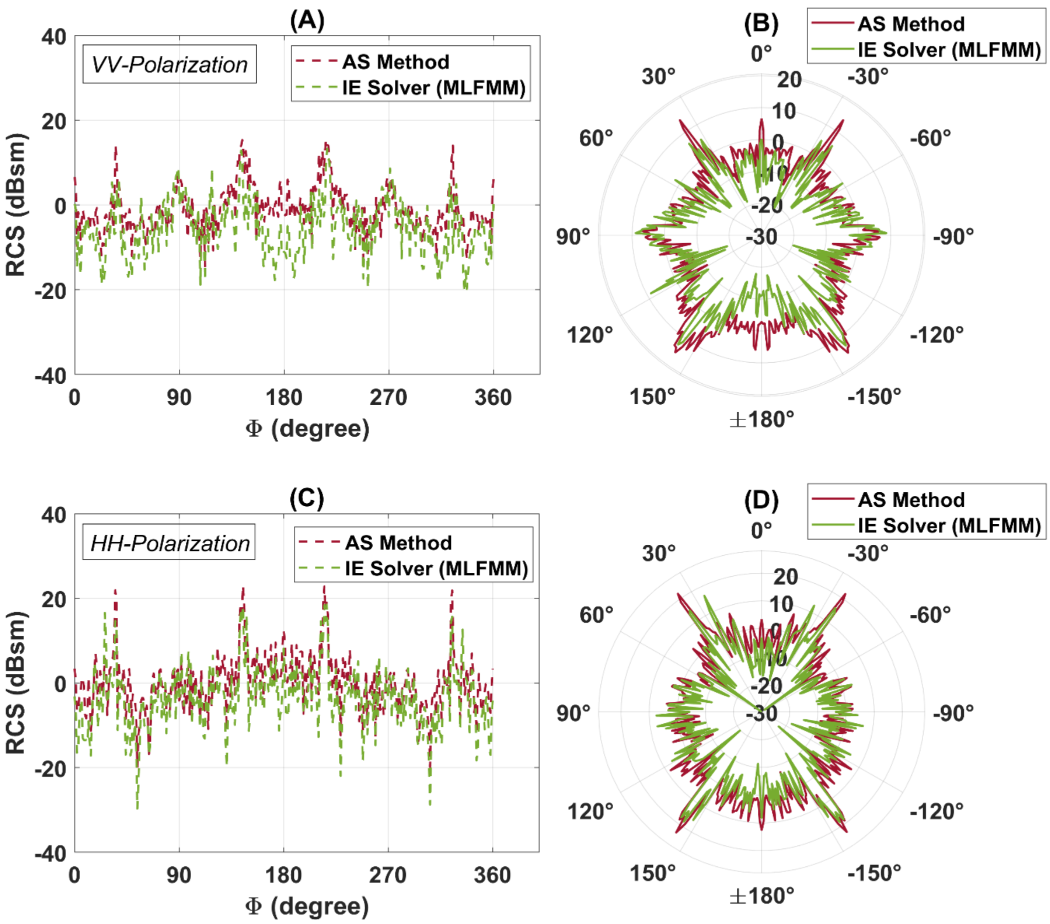

Figure 2. Linear and polar plots of RCS simulation results of B-2 aircraft at 300 MHz with 1° resolution, (A & B) VV-polarization; (C & D) HH-polarization. Results compare two solver methods: Asymptotic Solver (AS) and Integral Equation-Multilevel Fast Multipole Method (MLFMM). The AS method exhibits elevated RCS values due to its high-frequency approximation, which simplifies scattering and limits resolution of interference and shadowing effects. In contrast, the MLFMM method provides RCS estimates by solving full-wave equations, though at a higher computational cost

2.2 *RCS simulation results*

Following model validation, we simulated the full-aspect monostatic RCS of the B-2 Spirit aircraft, modeled with a wingspan of 52.37 m and a length of 21.49 m. The radar line-of-sight was defined in spherical coordinates with elevation angle $\theta = 90°$ and azimuth ϕ swept from 0° to 360° capturing full *x*-*y* plane coverage. Simulations were performed in CST Studio Suite using the Asymptotic Solver, due to lesser time of simulations with higher data resolution, at frequencies of 200, 300 and 400 MHz for both VV and HH polarizations, with an angular resolution of $\Delta\phi = 0.1°$. Initially, the aircraft was modeled with a Perfect Electric Conductor (PEC) coating to establish a geometric scattering baseline. This setup reflects all incident electromagnetic energy thus accentuating structural scattering mechanisms such as specular reflections and multiple bounces. CST's Asymptotic Solver based on the SBR method calculates RCS via ray tracing and applies PO to estimate surface currents. It neglects diffraction and low-frequency resonance effects leading to exaggerated peaks where geometric optics GO reflections dominate. Subsequently, the model was coated with a RAM layer characterized as ferrite-based [37], with frequency-dependent complex permeability and fixed relative permittivity $\varepsilon = 12.5$. At 300 MHz [23, 25], the permeability was modeled as $\mu = 1.8 - j29.3$, while values at 200 MHz and 400 MHz were adjusted to $\mu = 1.8 - j39.3$ and $\mu = 1.8 - j19.3$, respectively. The RAM layer was assigned a thickness of 2 mm, and simulations were repeated under identical conditions.

The resulting RCS profiles, as shown in Figure 3, demonstrate distinct frequency and polarization dependencies. At 200 MHz, the longer wavelength increases surface wave penetration leading to moderate RAM effectiveness and higher

RCS due to enhanced surface current coupling. At 400 MHz, the shorter wavelength interacts more strongly with small geometric features but the lower loss tangent reduces RAM absorption yielding intermediate RCS suppression. The most pronounced RCS reduction occurs at 300 MHz, where the imaginary part of μ reaches its peak, maximizing absorptive attenuation of incident rays. Polarization effects are also evident. VV-polarization, being aligned with surface-normals enhances specular returns particularly near wing edges. HH-polarization interacts more with tangential components and exhibits smoother scattering profiles with less pronounced peaks owing to its sensitivity to distributed surface currents. This comparative analysis highlights the interplay between frequency, polarization, material properties and geometric optics in shaping the RCS of stealth aircraft. For subsequent modeling, we selected 300 MHz as the reference frequency due to its optimal balance between scattering behavior and RAM absorption performance.

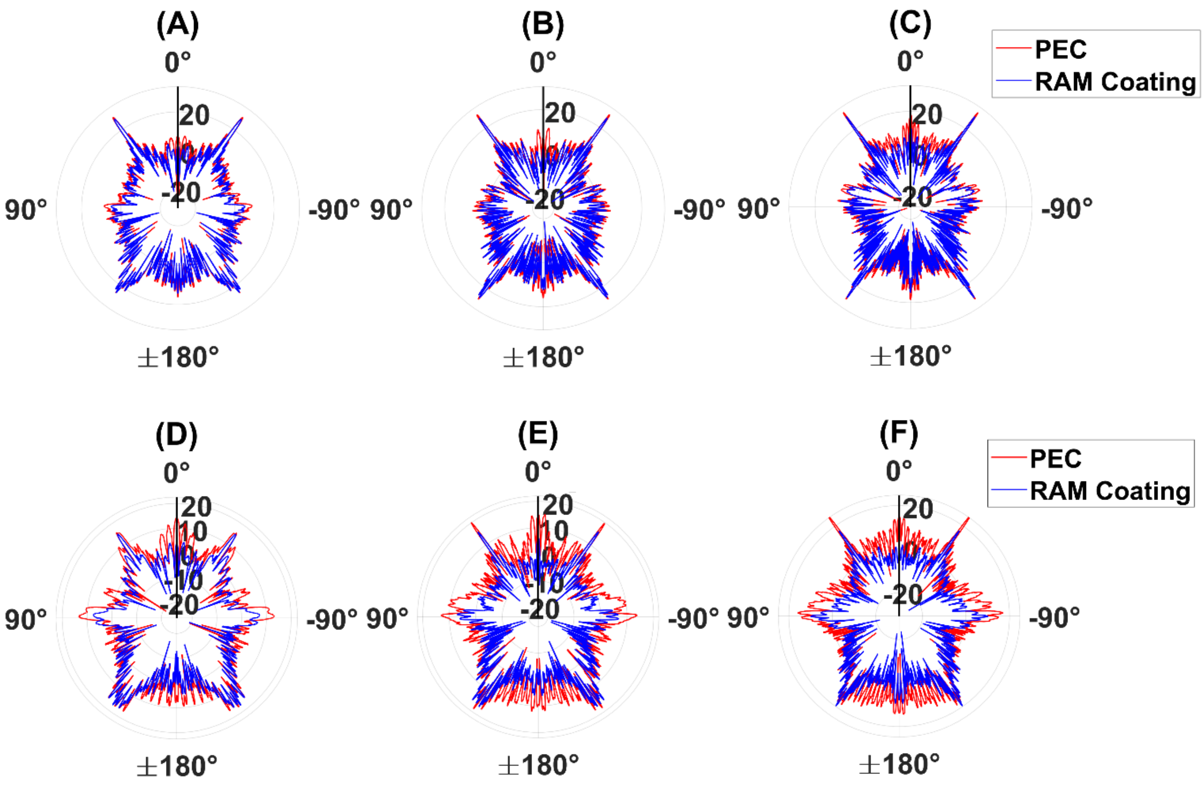

Figure 3. Radar cross section (dBsm) simulation profiles of B-2 Spirit stealth aircraft model coated with PEC & RAM in the *x*-*y* plane, (A) HH-200MHz; (B) HH-300MHz; (C) HH- 400MHz; (D) VV-200MHz; (E) VV-300MHz; (F) VV-400MHz, Reduced RCS levels can be observed with RAM coating

To extend the broadside ($\theta = 90°$) RCS analysis, we conducted additional simulations at 300 MHz with varying incidence angles to identify angular scattering hotspots as shown in Figure 4. The AS Method in CST Studio Suite, based on the SBR method was used to compute the monostatic RCS of the RAM-coated B-2 Spirit. The incidence angle θ was swept from 30° to 150° in 0.4° increments, while azimuth ϕ was varied from 0° to 180° with a step of 0.2°, generating high-resolution RCS heat maps for both HH and VV polarizations as shown in Figure 5. The SBR method models wave propagation as ray trajectories and estimates induced surface currents on illuminated facets using PO and GO methods. These currents are integrated to compute scattered fields with specular and first-order reflections dominating the response. Importantly, the solver does not account for diffraction and creeping waves scattering [38] making it particularly sensitive to surface orientation and incidence geometry. The resulting RCS maps reveal localized hotspots at specific θ values. For HH-polarization as in Figure 5A,B, enhanced scattering occurs at $\theta \approx 32.8°$ and 148°, while for VV-polarization (Figure 5C,D), peaks are observed at $\theta \approx 30°$, 31.2°, and 147.2°. These hotspots align with geometric transitions on the aircraft such as wing-root junctions and trailing edges which satisfy specular reflection conditions at particular incidence angles. VV-polarization, which emphasizes normal surface components leading to sharper angular dependence whereas HH-polarization includes tangential components and grazing reflections, producing broader angle response due to extended surface interactions. To further validate these observations, detailed 2D RCS histograms are also provided in Figure 5B,D. These visualizations enable analysts to identify angle-dependent scattering centers that may otherwise be overlooked in conventional polar plots. By correlating angular sectors with enhanced backscatter signatures, these visual tools could support operational decisions such as radar placement, polarization selection and their utility becomes especially evident in strategic stealth analysis, where target signatures are deliberately minimized and detection windows could be narrow.

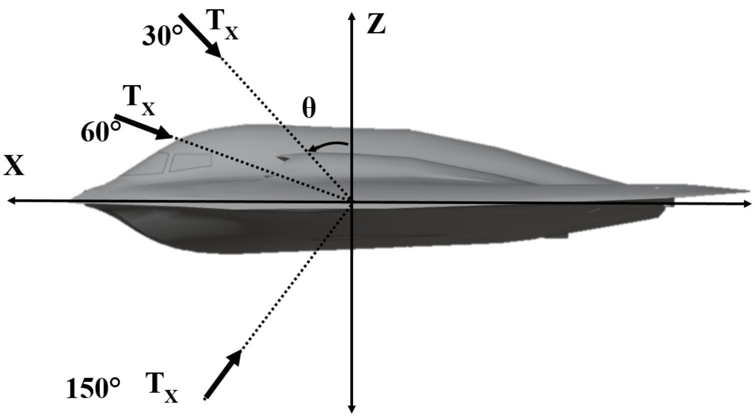

Figure 4. Incidence angles used for illumination of the B-2 Spirit aircraft to simulate the RCS profiles other than broadside incidence

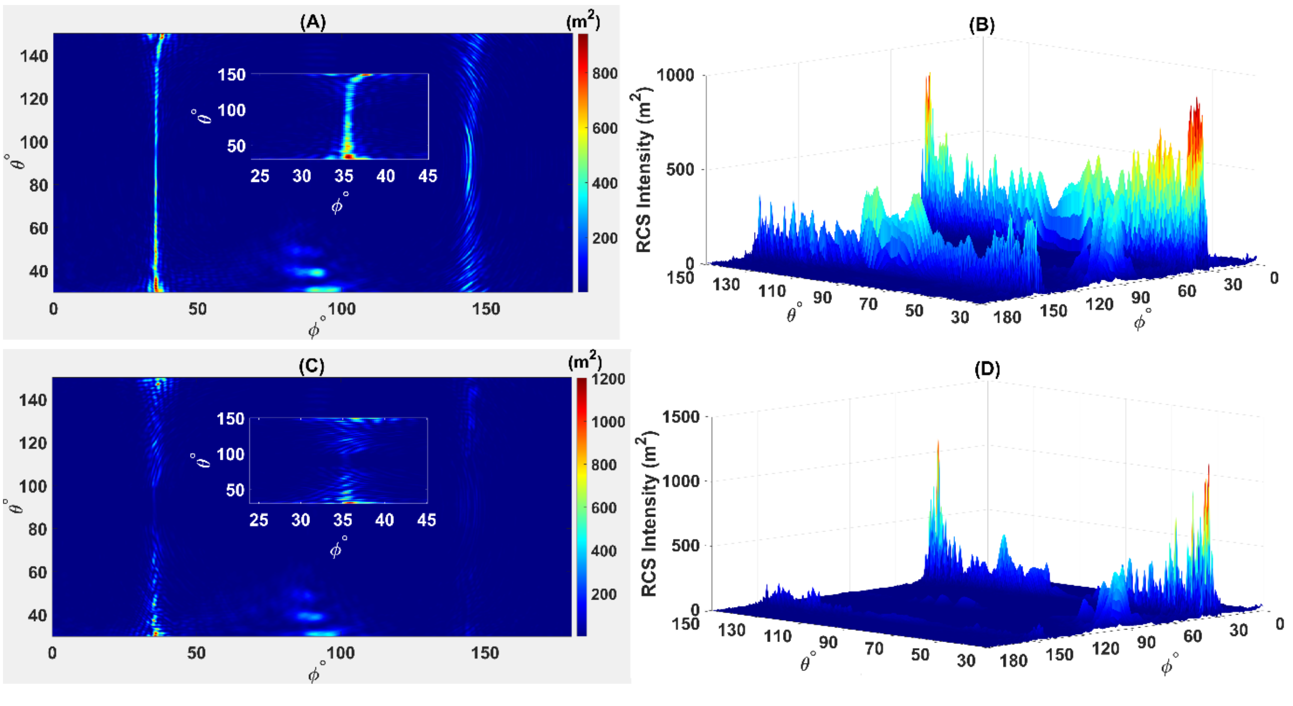

Figure 5. Heat-maps for RCS simulations of B-2 Spirit aircraft, (A) Heat-map from simulation results as θ is varied from 30° to 150° for HH; (B) 2-D histogram of heat-map for HH; (C) Heat-map simulation results for $\theta = 30°$ to 150° and $\phi = 0° \sim 180°$ for VV; (D) 2-D histogram of heat-map for VV. Strong RCS scattering hotspots are visible at different θ angles (inset of (A) & (C)) as the direction of the incident wave is changed for both polarizations. Corresponding high RCS peaks are visible in 2D histograms for θ equals to 32.8° & 148° for HH & at 30°, 31.2° & 147.2° for VV. The 2-D histograms in panels (B) and (D) were generated using angular bin sizes of $\Delta\theta = 0.4°$ and $\Delta\phi = 0.2°$, consistent with the simulation sweep resolution

Subsequently, RCS is further calculated at these illumination angles using the corresponding HH & VV θ-values as shown in Figure 6. Enhanced RCS levels are clearly observed, when aircraft is illuminated other than $\theta = 90°$. The emergence of these hotspots aligns with structural features such as trailing edge of wingtips of this stealth aircraft. This underscores the role of angular geometry and polarization in shaping the radar signature of stealth aircraft. From a system design perspective, these findings support the use of OTH or high-incidence angle bistatic radars, where the target is illuminated from above or at grazing angles exposing otherwise suppressed scattering features of the low-observable targets. While this study could provide valuable insights into stealth performance under above mentioned constraints, frequency-dependent scattering mechanisms such as surface wave penetration & diffraction spreading are not fully explored here. These are highly likely to influence hotspot formation and RCS peak shifts under different conditions. A more comprehensive frequency sweep and material variation study is proposed as a future publication to extend these findings.

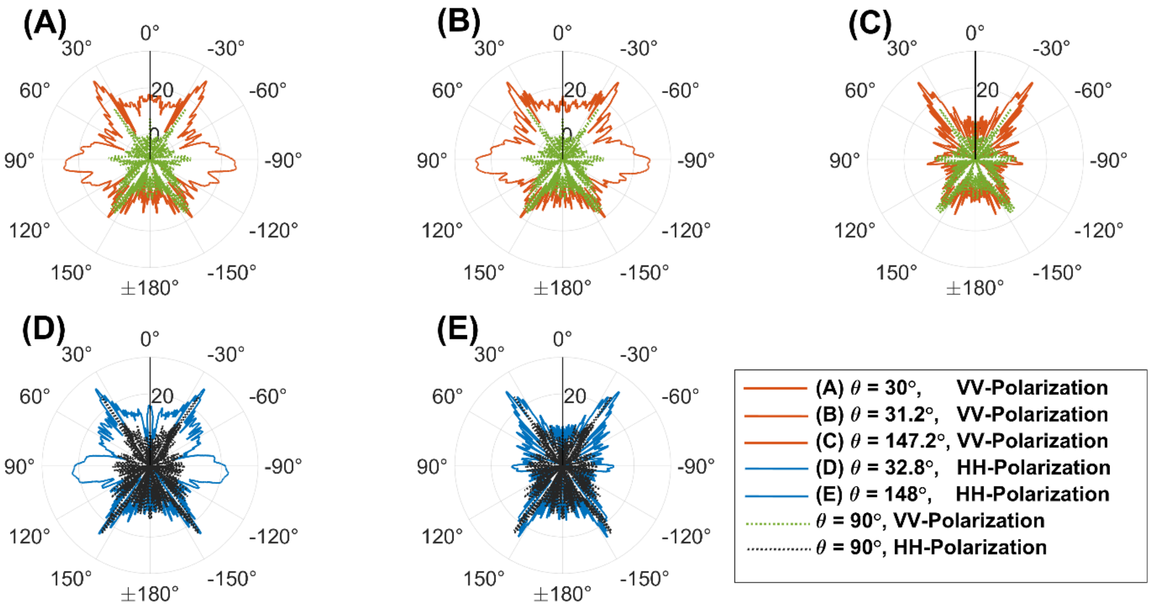

Figure 6. Monostatic Radar cross section simulations of B-2 Spirit aircraft, (A) θ = 30°-VV; (B) θ = 31.2°-VV; (C) θ = 147.2°-VV; (D) θ = 32.8°-HH; (E) θ = 148°-HH, Enhanced RCS levels can be observed as aircraft is illuminated from top in both HH & VV in comparison to 90° illuminations

While the B-2 Spirit aircraft is engineered to suppress monostatic radar returns through stealth shaping and RAM, bistatic radar configurations can reveal angular scattering features not observable from direct backscatter. To analyze these effects, bistatic RCS simulations were performed using CST Studio Suite's AS Method at 300 MHz with RAM coating. Illumination angles (θ) were varied from 30° to 80° in 1° increments while azimuth (ϕ) was swept from 0° to 360° as depicted in Figure 7. The receiver was fixed at $\theta = 160°$ representing a ground-based observation point in a forward-scatter or over-the-horizon scenario. Here, θ denotes the polar angle measured with respect to the positive z-axis of the target-centered coordinate system. Therefore, the transmitter sweeps of $\theta = 30°$ to 80° represents elevated or upper-hemisphere incidence, while the receiver direction at $\theta = 160°$ represents a lower-hemisphere observation direction. This bistatic configuration is used as a controlled scattering-geometry study to examine how elevated illumination can expose angular scattering features that may not be dominant in conventional monostatic broadside observation. It should not be interpreted as a complete propagation model of a specific deployed OTH radar. Rather, it is motivated by high-incidence and skywave/forward-scatter concepts, where a ground-based transmitted wave may arrive at the target along an elevated path after atmospheric or ionospheric propagation, while a spatially separated receiver observes from a different look direction. Complementary lower-hemisphere transmitter illumination cases may also be relevant for ground-based bistatic systems and are identified as a useful extension for future work. The resulting bistatic heat maps, as shown in Figure 8, demonstrate distinct polarization-dependent behavior. For VV-polarization (Figure 8C,D), the maximum RCS occurs at $\theta = 30°$, corresponding to a bistatic angle of 130°, where the transmitter-target geometry satisfies a strong specular condition. VV-polarization emphasizes normal reflections and at this configuration, energy is efficiently directed toward the fixed receiver. In contrast, HH polarization (Figure 8A,B) peaks at $\theta = 67°$ corresponding to a bistatic angle of 93°. HH aligns with tangential surface currents and grazing incidence leading to stronger scattering at moderate bistatic angles where these interactions dominate. Beyond this point, HH RCS diminishes due to the absence of modeled creeping waves and reduced PO efficiency at large angles.

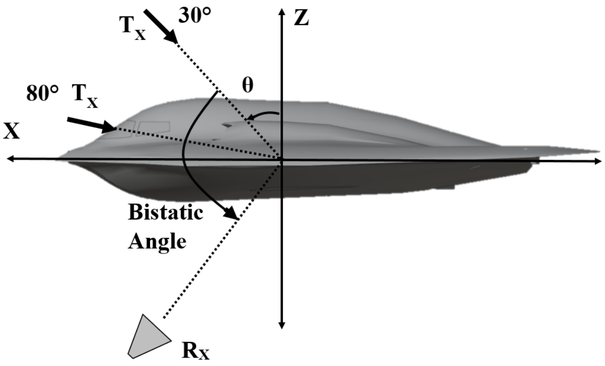

Figure 7. The transmitter incidence angles $\theta = 30°–80°$ represent elevated/upper-hemisphere illumination, while the fixed receiver angle $\theta = 160°$ represents lower-hemisphere observation; this geometry is used as a controlled bistatic scattering configuration rather than a complete OTH propagation model

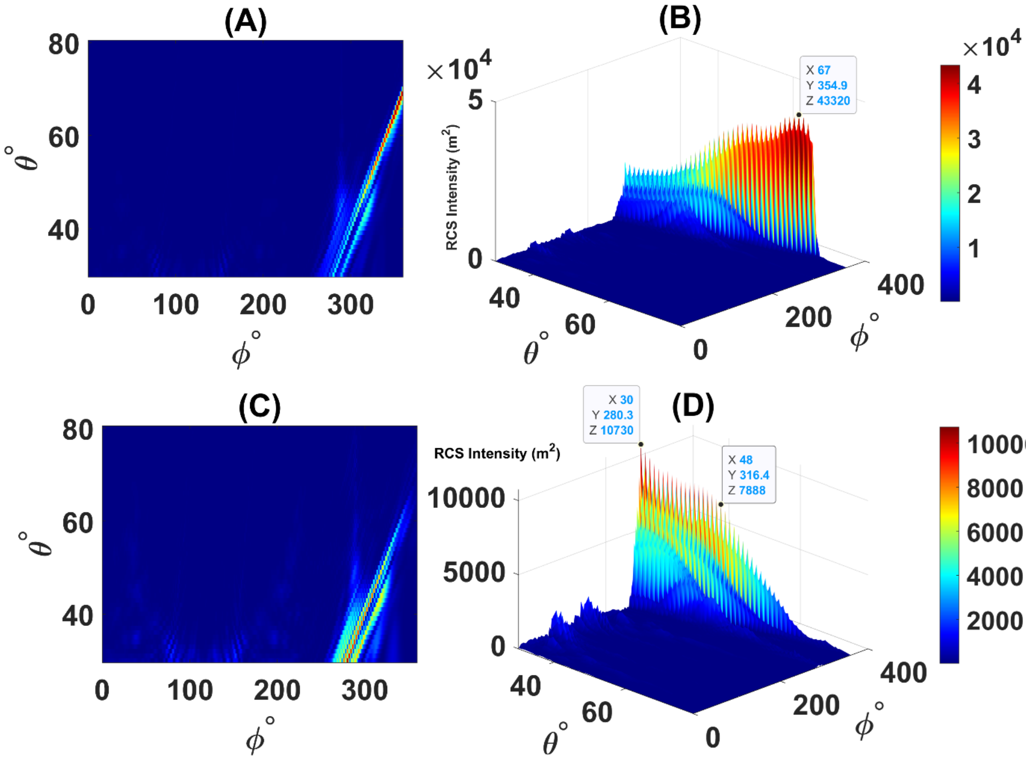

Figure 8. Bistatic Heat-maps for RCS simulations of B-2 Spirit aircraft, (A) Heat-map from simulation results as θ is varied from 30° to 80° for HH; (B) 2-D histogram of heat-map for HH; (C) Heat-map results for $\theta = 30°$ to 80° and $\phi = 0° \sim 360°$ for VV; (D) 2-D histogram of heat-map for VV. Strong RCS scattering hotspots are visible at different bistatic angles highlighting the importance of incident wave polarizations

The bistatic RCS profiles, as illustrated in Figure 9 against corresponding bistatic angles, also exhibit spatial asymmetry, attributable to the non-reciprocal observation geometry. In bistatic systems, the transmitter and receiver observe different surface regions of the target resulting in unequal angular contributions to the scattered field. The SBR based solver amplifies this asymmetry by only accounting for illuminated specular reflective surfaces relative to the transmitter direction. These results confirm that bistatic radar configurations can exploit angular scattering behaviors otherwise suppressed in monostatic detection. They further underscore the role of polarization selection and angular placement in optimizing stealth detection strategies under realistic field geometries.

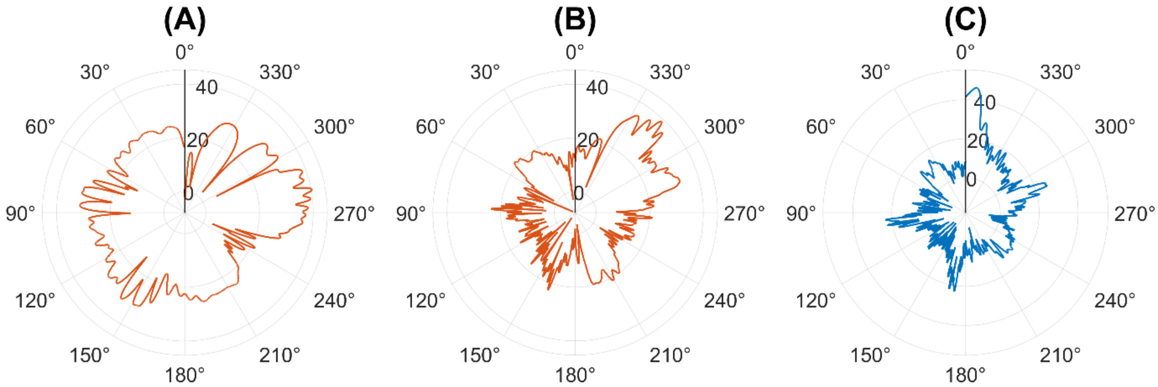

Figure 9. Bistatic RCS (dBsm) simulations of B-2 Spirit aircraft, (A) bistatic angle = 130°-VV; (B) bistatic angle = 112°-VV; (C) bistatic angle = 93°-HH

2.3 *RCS statistical modelling*

To facilitate probabilistic detection analysis, the monostatic and bistatic RCS profiles of the B-2 Spirit aircraft are statistically modeled using simple unimodal probability distributions. Given the inherently non-Gaussian and aspect-dependent nature of RCS data, particularly for stealth platforms, we select three commonly used flexible models which are WEIB, LOGN and β distributions. This choice is motivated by the heavy-tailed and skewed nature of the RCS statistics. As we can observe from Table 1 that std values are exceeding mean values indicating a strong right-skew and a long-tail behavior. Such characteristics are well-suited to WEIB or β distributions. Moreover, these distributions offer computational simplicity and are widely used in radar detection theory. To model local fluctuations, the RCS profiles are segmented into 10° angular windows. For monostatic data, we consider the symmetric range $\phi = 0°–180°$, resulting in 18 non-overlapping windows each modeled using 100 samples ($\Delta\phi = 0.1°$). For bistatic data, asymmetry requires modeling over the full $\phi = 0°–360°$ range, yielding 36 segments. This approach reflects practical radar field-of-view constraints where detection may be prioritized over narrow angular sectors in operational settings. Furthermore, each segment's RCS data is statistically fitted using all three distributions and the best-fit model is selected via the Kolmogorov-Smirnov (KS) test based on the maximum p-value. Parameter estimation is performed using Method of Moments (MoM) or Maximum Likelihood Estimation (MLE) depending on distribution characteristics. Equation (3), (4) & (5) represents Probability Density Function (PDF) of WEIB, LOGN and β-distributions respectively.

$$f(\sigma) = (\frac{k}{\lambda})\left(\frac{\sigma}{\lambda}\right)^{k-1} \exp -(\frac{\sigma}{\lambda})^{k} \tag{3}$$

$$f(\sigma) = \frac{\exp\left\{\frac{-\ln^2(\frac{\sigma}{\alpha})}{4\ln(\rho)}\right\}}{\sigma\left[4\pi\ln(\rho)\right]^{\frac{1}{2}}} \tag{4}$$

$$f(\sigma) = (\frac{\Gamma(a+\ b)}{\Gamma(a)\Gamma(b)})(\sigma)^{a-1}(1-\sigma)^{b-1} \tag{5}$$

whereas σ represents RCS and (k, λ), (α, ρ) & (a, b) represents the parameters of WEIB, LOGN and β-distributions. As an example we select WEIB distribution for estimation of parameters using MoM. The MoM is defined by equating the sample moments $\mu_j = \frac{1}{n}\sum_{i=1}^{n}\sigma_i^j$ and moment generating function of WEIB given as $M_j(t) = \lambda^j\Gamma\left(1+\frac{j}{k}\right)$, where j and $\Gamma(\cdot)$ represents j^{th} theoretical moment and gamma function respectively. Theoretical moments function using RCS data is approximated, when second sample moment is divided by square of the first sample moment as given in (6):

$$\frac{n\sum_{i=1}^{n}\sigma_i^2}{[\sum_{i=1}^{n}\sigma_i]^2} \approx \frac{\Gamma\left(1\ +\ \frac{2}{\widehat{k}}\right)}{\Gamma^2\left(1\ +\ \frac{1}{\widehat{k}}\right)}. \tag{6}$$

We can use the root finding techniques such as bisection or Newton-Raphson method to estimate $\widehat{k}$ from (6). And then finally we can other WEIB parameter as:

$$\hat{\lambda} = \frac{\overline{\sigma}}{\Gamma\left(1\ +\ \frac{1}{\widehat{k}}\right)}. \tag{7}$$

Moreover, we can estimate parameters a and b of β distribution using MLE method. Let $\sigma_1, \sigma_2, \ldots, \sigma_n$ denote the normalized RCS samples within [0, 1]. The log-likelihood function for β distribution is:

$$\ln f\,(\sigma|a,b) = n\,[\ln\Gamma(a+b) - \ln\Gamma(a) - \ln\Gamma(b)\,] + (a-1)\sum_{i=1}^{n}\ln\sigma_i + (b-1)\sum_{i=1}^{n}\ln(1-\sigma_i)\,. \tag{8}$$

To estimate the parameters using MLE, we solve the differential equations $\frac{\partial\ln f(\sigma|a,b)}{\partial a} = 0$ and $\frac{\partial\ln f(\sigma|a,b)}{\partial b} = 0$, and we get:

$$\psi(a) - \psi(a+b) = \left(\frac{1}{n}\right)\sum_{i=1}^{n}\ln\sigma_i \tag{9}$$

$$\psi(b) - \psi(a+b) = \left(\frac{1}{n}\right)\sum_{i=1}^{n}\ln(1-\sigma_i) \tag{10}$$

where $\psi(.)$ is a digamma function. Equations (9) and (10) can be solved by forming a Jacobian matrix and then using Newton-Raphson method to estimate a and b of β distribution.

2.4 *Probability of detection*

After fitting segment-wise RCS data with appropriate statistical distributions, we evaluate the P_d using a Monte Carlo simulation framework. This approach numerically estimates P_d by simulating signal and noise realizations over a large number of trials and computing the fraction of times the received signal exceeds a predefined detection threshold. In each Monte Carlo trial, a random signal sample S_x is drawn from the fitted RCS distribution for the corresponding angular window. This value is then scaled to reflect the desired Signal-to-Noise Ratio (SNR) modeling a target return under specific power conditions. Simultaneously, a noise sample N_x is generated from a standard Gaussian distribution (zero-mean, unit-variance), representing white thermal noise at the receiver. Detection is based on a non-coherent energy detection scheme, where the squared magnitude of the received signal-plus-noise is compared against a constant threshold Y_B. If the energy exceeds this threshold, detection is declared for that trial. Mathematically, the estimated probability of detection is

$$P_D = \sum_{i=1}^{trials} \left(|S_x + N_x|^2 \right) \geq \frac{Y_B}{trials} \tag{11}$$

whereas S_x, N_x and Y_B are signal, noise and threshold (also called bias value), respectively.

3. Results and discussion

Figure 10 presents the required SNR to achieve 90% P_d ($P_d = 0.9$) for different 10° angular sectors in the monostatic configuration across multiple illumination angles and polarizations. The RCS data is segmented from $\phi = 0°$ to 180° with $\theta = 30°$, 31.2° and 147.2° for VV-polarization (Figure 10A–C) and with $\theta = 32.8°$ and 148° for HH-polarization (Figure 10C,D). Also, RCS profile with $\theta = 90°$, representing a broadside radar view, is presented for comparison. The detection threshold $Y_B = 13.82$ is used for all calculations [39], corresponding to a false alarm probability of $P_{FA} = 10^{-6}$. Each sector's RCS is modeled using best-fit statistical distributions (WEIB, LOGN or β) and the corresponding P_d is estimated via Monte Carlo simulations using one pulse per trial.

The analysis reveals that the 90°–100° sector consistently requires the lowest SNR to reach 90% detection, particularly for high-incidence illuminations ($\theta = 30°$, 31.2° for VV and 32.8° for HH) from above. This behavior is explained by the wing geometry and structural composition of the B-2 Spirit, where the wing trailing edges and root junctions produce specular returns under certain incidence conditions. Under the AS Method, which uses the SBR technique with PO and GO approximation, surface currents are induced only on large illuminated facets. These currents are strongest when the incidence angle aligns with planar features whose orientation satisfies specular reflection back toward the radar. The trailing edges of the B-2 especially in the 90°–100° sector, present sloped surfaces that can act as retroreflective planes under oblique top-down illumination causing energy concentration in these sectors. Since PO ignores edge diffraction and creeping waves the solver favors first-order geometric optics returns which are maximized here. Consequently, these sectors exhibit enhanced backscatter and thus stronger signal returns, reducing the required SNR to achieve the P_d threshold. This highlights a vulnerability in stealth shaping under elevated radar configurations. In contrast, when the aircraft is illuminated from below, SNR requirements remain uniformly high across all 10° sectors. This is attributed to the intentional stealth shaping of the aircraft's ventral (bottom) surface, where no protruding vertical surfaces exist, engine inlets and exhausts are buried internally and RAM coatings and edge alignments minimize surface normal exposure. Moreover, under bottom-up illumination, no significant portion of the trailing edge or wing junctions satisfy the specular alignment condition needed for PO-induced strong returns. As a result, backscattered energy remains low and no angular window presents a detection advantage thereby requiring higher SNR for detection across the entire azimuth range as presented in Figure 10C,E for $\theta = 147.2°$ and 148°. This asymmetry in detection performance reflects the non-uniform RCS shaping of the B-2, where the lower surface is specifically designed for ground-based radar evasion while the upper surface, though stealthy is more exposed under top-down or elevated illumination scenarios.

Figure 11A,B depict the SNR values required to achieve 90% P_d across the full 360° azimuthal RCS profile for the B-2 Spirit aircraft in bistatic configuration using VV polarization. The two cases correspond to bistatic angles of 130° and 112°, derived from illumination angles of 30° and 48° (illumination angle $\theta = 48°$, bistatic angle is $160° - 48° = 112°$), respectively. These angles were selected based on the observed RCS extremes in the bistatic heat maps (see Figure 8D), where $\theta = 30°$ yielded the highest bistatic RCS and $\theta = 48°$ corresponded to the lowest RCS levels. In both cases, AS Method was used to estimate the scattered fields.

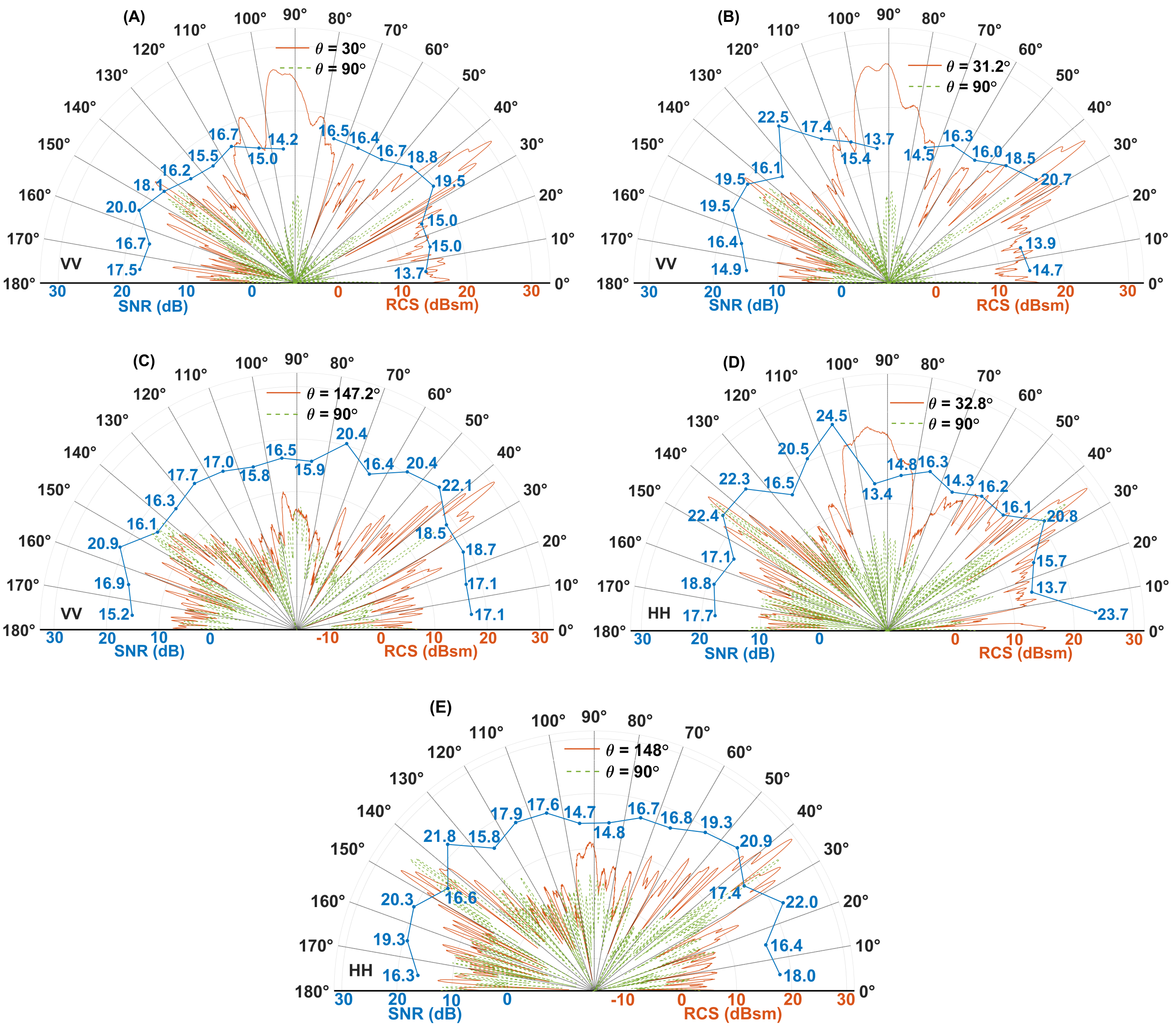

Figure 10. SNR (dB) values for RCS simulations of B-2 Spirit aircraft to achieve 90% probability of detection (P_d), $P_{fa} = 10^{-6}$, (A) VV-pol $\theta = 30°$; (B) VV-pol $\theta = 31.2°$; (C) VV-pol $\theta = 147.2°$; (D) HH-pol $\theta = 32.8°$; (E) HH-pol $\theta = 148°$. The sector spanning from 90° to 100°, corresponds the wing tips, requires the lowest SNR to achieve a 90% P_d, emphasizing the significance of the concentrated RF spectrum in this region. Sectors without SNR values did not pass the KS test for Weibull, Lognormal, and Beta distributions. SNR trends for bottom illumination in C & E exhibit a similar pattern, highlighting the sophisticated design of the B-2 Spirit aircraft in minimizing detection under varying illumination conditions

As seen in Figure 11A, the bistatic configuration with a 130° angle results in significantly enhanced RCS levels in the first and second quadrants (0°–180° azimuth) corresponding to increased backscattered energy toward the fixed receiver. These high RCS values coincide with reduced SNR requirements, down to 14–15 dB in several sectors to achieve 90% detection. This is expected as PO-based SBR methods emphasize specular returns; when the bistatic angle approaches the forward scattering region, surface patches on the B-2's upper side could become more favorably aligned with both transmitter and receiver increasing the effective reflection. The B-2's blended wing-body shape while effective in reducing monostatic reflections through careful edge alignment and shaping still exhibits anisotropic scattering. In bistatic scenarios, the symmetry that exists in monostatic profiles (where $\theta = 30°$ illumination produces symmetric lobes around $\phi = 0°–180°$ & 180°–360°) breaks down because the observation point (receiver) is now fixed at a different angular position. This asymmetry in receiver location disrupts the equal backscatter pattern, revealing sectors with either enhanced or diminished energy returns. In contrast, Figure 11B, representing the lower bistatic angle of 112° shows fewer high-RCS sectors. Here, the receiver lies closer to the transmitter, reducing angular separation and diminishing specular reflection contributions. This configuration limits the number of surface patches aligned with the bistatic scattering direction producing weaker returns and demanding higher SNR (approaching 17–18 dB) for 90% detection across most sectors. The comparison with the monostatic case in Figure 11C further confirms these trends. While monostatic illumination at $\theta = 30°$ yields symmetric scattering and moderate RCS levels, it generally demands higher SNR for detection compared to the 130° bistatic case, except for sectors where trailing-edge features are observed. This highlights the key advantage of bistatic configurations, by adjusting the receiver location, bistatic systems can exploit geometrical alignments that are less accessible to monostatic radars revealing hidden or suppressed scatterers and improving detection probabilities reinforcing the need for holistic RCS analysis beyond traditional monostatic assumptions.

Figure 11. SNR (dB) values for RCS simulations of B-2 Spirit aircraft to achieve 90% probability of detection (P_d), $P_{fa} = 10^{-6}$, (A) bistatic case for illumination $\theta = 30°$-VV; (B) bistatic case for illumination $\theta = 48°$-VV; (C) monostatic case for illumination $\theta = 30°$ -VV, enhanced RCS levels in different sectors require low SNR values. Sectors without SNR values did not pass the KS test for Weibull, Lognormal, and Beta distributions

3.1 *Entropy based detection complexity index*

To enhance the interpretability of radar detection results and uncover deeper insight into sector-wise detectability of stealth targets, we propose a Shannon entropy-derived metric termed the Entropy-based Detection Complexity Index (EDCI). This index complements the P_d by capturing how uniformly or non-uniformly the RCS is distributed within a given angular window. While previous section focused on identifying sectors with lower SNR requirements to achieve 90% P_d they did not quantify whether the scattering patterns within these sectors are deterministic or highly variable. EDCI fills this analytical gap by characterizing the underlying RCS distributions based on Shannon entropy. Let the angular domain $\phi \in [0°–180°]$ (monostatic case) and $\phi \in [0°–360°]$ (bistatic case) be partitioned into N non-overlapping angular windows of 10° resolution. For each window w_j, we define a discrete probability distribution over RCS magnitudes σ using normalized histogram binning and denote the RCS-based histogram for window w_j by $p_i^{(j)} = \frac{\text{Number of samples in bin } i}{\text{Total samples in the window } j}$, $i = 1, 2, \ldots, B$ where B is the number of bins. For each window w_j the entropy is computed as:

$$H(w_j) = -\sum_{i=1}^{B} p_i^{(j)} \log_2 p_i^{(j)}. \tag{12}$$

To ensure comparability across sectors and bin counts, we normalize the entropy to obtain a dimensionless index as:

$$H_{norm}(w_j) = \frac{H(w_j)}{\log_2 B}. \tag{13}$$

This normalized entropy values lies in the interval [0, 1], where $H_{norm} \approx 0$ implies low uncertainty scattering while $H_{norm} \approx 1$means highly diffused and unpredictable scattering. We validated the EDCI against three cases as shown in Figure 12. Figure 12A,B depicts monostatic illumination at $\theta = 30°$ and 147.2° catering for both top and bottom illumination. The corresponding entropy values are mentioned in each angular sector. This entropy framework is directly integrated with our earlier P_d results. In particular, we can observe that angular sectors that required lower SNR to achieve 90% P_d also exhibit lower entropy indicating both favorable detection characteristics and stable scattering behavior. Conversely, high-entropy sectors produce transient peaks in RCS but do not yield low SNR values due to scattering variability. We try to justify this phenomenon through classical radar detection and scattering principles: sectors with low EDCI indicate multiple fluctuating scatterers distributed spatially which enhance detection reliability via spatial diversity and increase the likelihood of strong echo returns. Conversely, high-entropy sectors can be characterized by sparse or dominant single-scatterer returns provide less spatial diversity causing the radar to require higher SNR to maintain detection confidence. This entropy-based framework thus offers a statistically grounded method to pre-screen detection difficulty across angular sectors reducing reliance on computationally expensive simulations. Moreover, it allows for adaptive radar resource allocation by prioritizing sectors based on their structural complexity, which has practical implications in the design and deployment of cognitive radar systems for stealth aircraft detection.

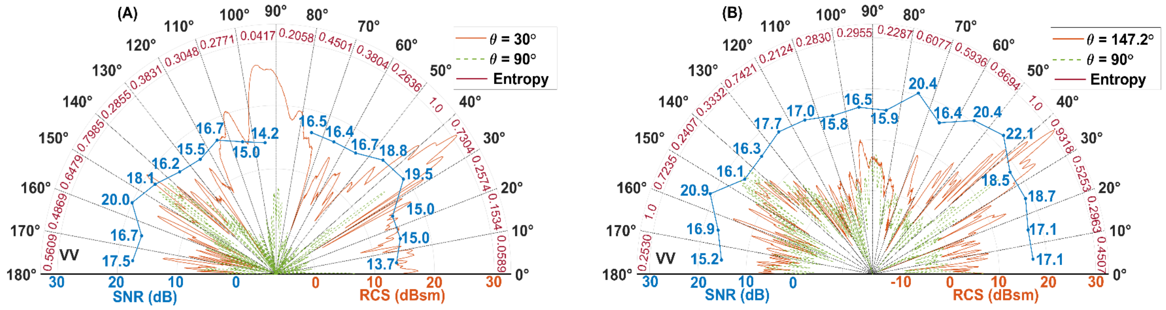

Figure 12. Monostatic RCS simulation profiles of B-2 spirit aircraft for VV-polarization, (A) $\theta = 30°$- top illumination; (B) $\theta = 147.2°$-bottom illumination, lower entropy values can be observed with sector having low SNR values depicting low variability in scattering patterns

4. Conclusion

This research presents a comprehensive evaluation of the B-2 Spirit's detectability by rigorously analyzing its radar cross section characteristics under varying illumination geometries and polarization modes within monostatic and bistatic radar frameworks. RCS heat map analyses reveal that maximum scattering occurs at specific off-broadside angles for both VV and HH such as 30°, 147.2° or 148° highlighting the strategic importance of angular illumination in improving detection performance. The signal-to-noise ratio variations observed between top and bottom illumination configurations further validate that high RF spectrum sectors require low signal-to-noise ratio up-till 13dB to achieve 90% probability of detection otherwise requiring more than 17dB. Through angular sector-wise statistical modeling and probabilistic detection analysis using Monte Carlo simulations, this study establishes a quantitative link between geometric scattering features and radar detection capability. The proposed methodology offers a scalable foundation for evaluating stealth target visibility under realistic radar conditions and serves as a valuable design and operational reference for enhancing future radar detection architectures.

Conflict of interest

The authors declare no conflicts of interest.

Abbreviations

AS	Asymptotic Solver
CAD	Computer-Aided Design
CEM	Computational Electromagnetics
CFIE	Combined Field Integral Equation
CST	CST Studio Suite
dBsm	Decibels relative to one square meter
DMU	Digital Mock-Up
EDCI	Entropy-based Detection Complexity Index
EFIE	Electric Field Integral Equation
GO	Geometrical Optics
HH	Horizontal-Horizontal Polarization
IE	Integral Equation
KS	Kolmogorov-Smirnov
LoGN	Log-Normal Distribution
MLE	Maximum Likelihood Estimation
MLFMM	Multilevel Fast Multipole Method
MoM	Method of Moments
OTH	Over-the-Horizon
Pd	Probability of Detection
PDF	Probability Density Function
PEC	Perfect Electric Conductor
PFA	Probability of False Alarm
PO	Physical Optics
RAM	Radar-Absorbing Material
RCS	Radar Cross Section
RF	Radio Frequency
SBR	Shooting and Bouncing Ray

SNR	Signal-to-Noise Ratio
UHF	Ultra-High Frequency
VHF	Very-High Frequency
VV	Vertical-Vertical Polarization
WEIB	Weibull Distribution

References

[1] E. F. Knott, J. F. Shaeffer, and M. T. Tuley, *Radar Cross Section*, 2nd ed. London, U.K.: Institution of Engineering and Technology, 2004, pp. 64-67. https://doi.org/10.1049/SBRA026E.

[2] G. T. Ruck, *Radar Cross Section Handbook*, 1st ed., vol. 1. New York, NY, USA: Springer, 1970, pp. 7-27.

[3] M. I. Skolnik, *Radar Handbook*, 3rd ed., vol. 3. New York, NY, USA: McGraw-Hill, 2008.

[4] F. E. Nathanson, J. P. Riley, and M. Cohen, *Radar Design Principles: Signal Processing and Environment*, 2nd ed. New York, NY, USA: McGraw-Hill, 1991, pp. 147-171.

[5] J. G. Van Bladel, *Electromagnetic Fields*, 2nd ed. Hoboken, NJ, USA: Wiley, 2007, pp. 563-582. https://doi.org/10.1002/047012458X.

[6] B. R. Mahafza, *Radar Systems Analysis and Design Using MATLAB*, 4th ed. New York, NY, USA: Taylor & Francis, 2022. https://doi.org/10.1201/9781003051282.

[7] R. Buderi, *The Invention That Changed the World: The Story of Radar from War to Peace*. Michigan, USA: Simon & Schuster, 1996.

[8] R. Colgren, D. Enns, and M. Jackson, "Structured singular value synthesis applied to the F-117A," *IFAC Proceedings Volumes*, vol. 29, no. 1, pp. 1008-1013, 1996. https://doi.org/10.1016/S1474-6670(17)57796-4.

[9] J. A. Adam, "How to design an 'invisible' aircraft," *IEEE Spectrum*, vol. 25, no. 4, pp. 26-31, 1988. https://doi.org/10.1109/6.4529.

[10] J. M. Dahm, "South China Sea military capability series: Air and surface radar," Johns Hopkins Applied Physics Laboratory, Jul. 2020. [Online]. Available: https://www.jhuapl.edu/sites/default/files/2022-12/AirandSurfaceRadar_v3.pdf. [Accessed Jun. 7, 2026].

[11] J. Marcum, "A statistical theory of target detection by pulsed radar," *IRE Transactions on Information Theory*, vol. 6, no. 2, pp. 59-267, 1960. https://doi.org/10.1109/TIT.1960.1057560.

[12] P. Swerling, "Probability of detection for fluctuating targets," *IRE Transactions on Information Theory*, vol. 6, no. 2, pp. 269-308, 1960 https://doi.org/10.1109/TIT.1960.1057561.

[13] R. E. Brcwia and R. R. Zirm, "The distribution of reflecting cross-sections of satellites," NRL Report 5615, May 1961. [Online]. Available: https://apps.dtic.mil/sti/tr/pdf/AD0259990.pdf. [Accessed Jun. 7, 2026].

[14] R. W. Kennedy, "The special and spectral characteristics of the radar cross-section of satellite-type targets," Air Force Avionics Lab., Tech. Rep. AFAL-TR-66-17, Mar. 1966. [Online]. Available: https://apps.dtic.mil/sti/pdfs/AD0830877.pdf. [Accessed Jun. 7, 2026].

[15] G. Pollon, "Statistical parameters for scattering from randomly oriented arrays, cylinders, and plates," *IEEE Transactions on Antennas and Propagation*, vol. 18, no. 1, pp. 68-75, 1970. https://doi.org/10.1109/TAP.1970.1139615.

[16] W. W. Weinstock, "Target cross-section models for radar systems analysis," Ph.D. dissertation, University of Pennsylvania, 1964.

[17] G. R. Heidbreder and R. L. Mitchell, "Detection probabilities for log-normally distributed signals," *IEEE Transactions on Aerospace and Electronic Systems*, vol. AES-3, no. 1, pp. 5-13, 1967. https://doi.org/10.1109/TAES.1967.5408709.

[18] D. P. Meyer and H. A. Mayer, *Radar Detection: Handbook of Theory and Practice*. New York, NY, USA: Academic Press, 1973, pp. 58-68. https://doi.org/10.1016/B978-0-12-492850-3.X5001-9.

[19] P. H. R. Scholefield, "Statistical aspects of ideal radar targets," *Proceedings of the IEEE*, vol. 55, no. 4, pp. 587-589, 1967. https://doi.org/10.1109/PROC.1967.5610.

[20] P. Swerling, "Recent developments in target models for radar detection analysis," *AGARD Conference*, May 1970. [Online]. Available: https://drive.google.com/drive/folders/12-DwiGecye7VqtRvxl5dstLYWgS81ea_?usp=sharing. [Accessed Jun. 7, 2026].

[21] S. O. Rice, “Mathematical analysis of random noise,” *Bell System Technical Journal*, vol. 23, no. 3, pp. 282-332, 1944. https://doi.org/10.1002/j.1538-7305.1944.tb00874.x.

[22] X. Xiaojian and P. Huang, “A new RCS statistical model of radar targets,” *IEEE Transactions on Aerospace and Electronic Systems*, vol. 33, no. 2, pp. 710-714, 1997. https://doi.org/10.1109/7.588496.

[23] Y.-R. Jeong, C.-S. Park, Y.-K. Ko, and J.-G. Yook, “Analysis of RCS of low observable aircraft in VHF band,” *International Journal of Antennas and Propagation*, vol. 2018, pp. 1-10, 2018. https://doi.org/10.1155/2018/5435837.

[24] J. Wang, J. Ye, and G. Hua, “Radar cross section statistical characteristics of stealth aircraft using the Weibull-generalized gamma mixture model,” *Microwave and Optical Technology Letters*, vol. 64, pp. 1500-1506, 2022. https://doi.org/10.1002/mop.33304.

[25] J. Wang, J. Ye, X. Wu, J. Sun, and G. Hua, “RCS statistical modeling of stealth targets based on fractional-order Legendre polynomials,” *IEEE Transactions on Aerospace and Electronic Systems*, vol. 59, no. 6, pp. 9807-9820, 2023. https://doi.org/10.1109/TAES.2023.3309613.

[26] S. S. M. Chung, C. Yi-Hsin, and C. Yu-Chou, “J9: Radar cross section analysis of stealth fighter design: Key factors and limitation of simulation,” *International Journal of Electrical Engineering*, vol. 23, pp. 201-214, 2016. https://doi.org/10.6329/CIEE.2016.6.02.

[27] W. Shi, X.-W. Shi, and L. Xu, “Radar cross section (RCS) statistical characterization using Weibull distribution,” *Microwave and Optical Technology Letters*, vol. 55, pp. 1355-1358, 2013. https://doi.org/10.1002/mop.27557.

[28] Simulia, “CST Studio Suite,” 2026. [Online]. Available: https://www.3ds.com/products/simulia/cst-studio-suite/. [Accessed Jan. 7, 2026].

[29] D. Lynch, *An Introduction to RF Stealth*. London, U.K.: Institution of Engineering and Technology, 2021, pp. 106-115. https://doi.org/10.1049/SBRA540E.

[30] H. Ling, R.-C. Chou, and S.-W. Lee, “Shooting and bouncing rays: Calculating the RCS of an arbitrarily shaped cavity,” *IEEE Transactions on Antennas and Propagation*, vol. 37, no. 2, pp. 194-205, 1989. https://doi.org/10.1109/8.18706.

[31] Simulia, “CST Studio Suite electromagnetic simulation solvers,” 2026. [Online]. Available: https://www.3ds.com/products/simulia/cst-studio-suite/electromagnetic-simulation-solvers/. [Accessed Jan. 7, 2026].

[32] J. Lindgren, “Evaluation of CST studio suite for simulation of radar cross-section,” M.S thesis, Department of physics, UmeåUniversity, Sweden, 2021.

[33] Northrop Grumman, “B-2 Spirit technical details,” 2026. [Online]. Available: https://www.northropgrumman.com/what-we-do/aircraft/b-2-stealth-bomber/technical-details. [Accessed Jan. 7, 2026].

[34] S. Lee, “The role of radar cross-section in advanced aircraft stealth design,” *Highlights in Science, Engineering and Technology*, vol. 120, pp. 283-289, 2024. https://doi.org/10.54097/b56kmh05.

[35] “Northrop B-2 Spirit,” Wikipedia, 2026. [Online]. Available: https://en.wikipedia.org/wiki/Northrop_B-2_Spirit. [Accessed Jan. 7, 2026].

[36] O. I. Sukharevsky and V. A. Vasilets, *Scattering Characteristics of Aerial and Ground Radar Objects*, 1st ed. Boca Raton, FL, USA: CRC Press, 2024, pp. 114-119. https://doi.org/10.1201/9781032676425.

[37] J. M. Griffin, J. K. Kinnu, and J. M. Colombi, “B-2 systems engineering case study,” 2007. [Online]. Available: https://apps.dtic.mil/sti/citations/ADA464771. [Accessed Jan. 7, 2026].

[38] P. Hogberg, “Shooting and bouncing rays method for radar signatures: a high-performance computing framework based on NVIDIA OptiX,” M.S thesis, Department of physics, UmeåUniversity, Sweden, 2024.

[39] B. R. Mahafza, *Introduction to Radar Analysis*, 2nd ed. New York, NY, USA: CRC Press, 2017. Available: https: //doi.org/10.1201/9781315119342.